ACS APPLIED ENGINEERING MATERIALS

pubs.acs.org/acsaenm Article

Alignment-Assisted Networks of Polyelectrolyte-Grafted Cellulose Nanocrystals

Yang Ge and Pinar Akcora*

Cite This: https://doi.org/10.1021/acsaenm.3c00378 Read Online

ACCESS | Metrics & More | Article Recommendations | Supporting Information

ABSTRACT: This study aims to understand the role of polyelectrolyte grafting on the dispersed cellulose nanocrystal (CNC) rods in water through measuring transport coefficients using depolarized and polarized dynamic light scattering and by measuring the viscoelastic properties using rheometer. Rotational and translational diffusivities are found to slow down with poly(acrylic acid) (PAA)-grafted chains compared to bare CNCs. Translational diffusion is shown to remain constant between pH 3 and 9, indicating the good dispersion and stability of PAA-grafted CNC suspensions. At the overlap solution concentration, chains play a significant role in bridging the CNC and form a network, as measured with the viscoelastic properties of neutral chains. When chains are ionized by altering the pH, the higher viscosity is measured because of the hydrogen bonding between ionized and un-ionized carboxylic groups, as previously demonstrated with PAA-grafted spherical nanoparticles. We further measured the viscoelastic response of PAA-grafted CNC after applying large steady shear. The results show that CNCs with long grafts presented enhanced viscoelastic moduli, and their critical strain value decreased after large shear flow application. Short grafts, in contrast to the long grafts, did not show any changes in the viscoelastic response under shear. These results indicate that the alignment-assisted networks of PAA-grafted CNC enable better entanglements between long grafted chains at the neutral state.

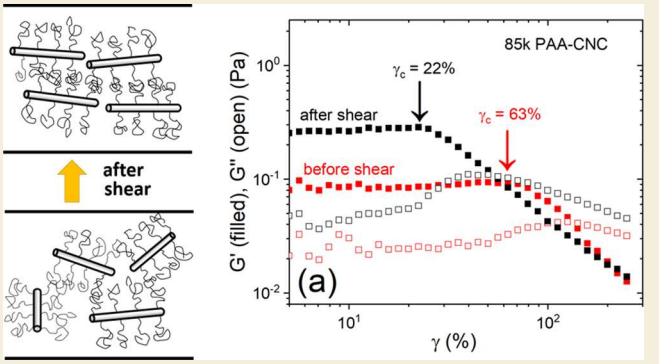

KEYWORDS: *cellulose nanocrystal, polyelectrolyte grafting, PAA, solution rheology, gelation*

INTRODUCTION

The high crystallinity and well-defined high aspect ratios of cellulose nanocrystals (CNCs) when used as fillers induce excellent mechanical properties in polymer matrices.[1−8] Like other colloidal rods, such as DNA fragments and chitin nanocrystals, CNC suspensions show interesting properties of a liquid crystal.[9,10] At above critical concentration, the CNC suspension phase separates into an upper isotropic phase and a lower anisotropic chiral nematic phase.[11−13] This concentration-dependent phase transition leads to research questions related to how addition of moieties, salts, or polymer influences the structural transition of CNCs.[14−16] CNC stabilization in suspensions and underpinning their interactions with other entities or particles enable their use for a wide range of applications, such as catalysis, self-healing membrane technologies, or conductive thin films.[17−21]

One strategy to alter the surface interactions and environment is by grafting polymer chains for applications related to lubrication,[22] adhesion,[23] or colloidal stabilization.[24−26] Polymer molecular weight, grafting density, and ionization degree govern the chain conformations. Poly(acrylic acid) (PAA) is a weak polyelectrolyte that can be ionized in water and has a highly negative charge density when all carboxyl groups dissociate. When the pH exceeds 4.5, PAA chains are partially ionized and form hydrogen bonds between ionized and un-ionized carboxyl groups.[27,28] The chemical bridging and entanglements of grafts create a weak network between the soft particles. At a high pH, the electrostatic repulsive forces of fully ionized chains generate a hydrated shell that could further hinder the interpenetration and hydrogen bonding between grafts.[29,30] PAA graft conformations with pH changes were studied in small-angle neutron scattering (SANS) previously in our group.[31] The viscosity changes of PAA-grafted spherical nanoparticle solutions were explained by the interparticle and intraparticle chain interactions, as investigated by rheological measurements and molecular dynamics simulations.[31]

The hydrodynamic alignment of CNC rods was previously studied for producing a structured ordered material.[32,33] For composite materials, understanding the hydrodynamic align-

Received: July 9, 2023
Revised: August 31, 2023
Accepted: September 7, 2023

ment of CNC rods in polymer matrices is critical for processing the concentrated suspensions.[32,34,35] This work is motivated by the elucidation of the effect of grafted polyelectrolyte on the viscoelastic properties of CNC rods. Here, we showed that PAA chains can be easily grafted on CNC surfaces at molecular weights that are much higher than those achieved on spherical nanoparticles. Our system is unique as the grafted chain conformations change with pH, which subsequently modifies the interactions between CNCs. Our intent is then to show that effective crowding of chains is attained through grafting the chains on CNC, and any viscoelastic changes of CNC suspensions in water are directly related to the CNC alignment and to the elasticity of entangled grafted chains. Thus, this work stands out from previous works where the flow-induced alignment of bare rods in polymer solutions has been investigated.[36,37] We propose that the high entanglement density of grafted PAA chains around the CNC may induce stronger particle interactions and higher viscoelastic moduli. We present rotational and translational diffusivities of these solutions at different pH values and then discuss the complex viscosities of the two batches of PAA-grafted CNC suspensions at overlap concentrations with the ionization of chains. These results are critical for understanding the transport of CNCs at overlap concentrations and the molecular weight effect on the viscoelastic properties of CNC rods with grafted chains at different ionization states. The rheological properties of PAA-grafted CNC suspensions are crucial for the engineering of drug delivery systems.

EXPERIMENTAL SECTION

PAA-grafted CNC samples listed in Table 1 were synthesized, and translational and rotational diffusion of these colloidal rods at different pHs were analyzed using dynamic light scattering (DLS). The rheological properties of solutions at the overlap concentrations of CNCs were measured to understand the role of ionization in interparticle interactions. The viscoelastic response of PAA-grafted CNC samples after steady-shear application was further used to explain the alignment of CNC fillers.

Table 1. Molecular Weights ($\bar{M}_n$) and Grafting Densities (σ) of PAA-Grafted CNC Samples

sample name	PAA $\bar{M}_n$ (kg/mol)	σ (chains/nm^2)
37k PAA−CNC	37	0.018
85k PAA−CNC	85	0.027
127k PAA−CNC	127	0.032

Preparation of PAA-Grafted CNC

CNCs extracted by the general hydrolysis of cellulose were purchased from CelluForce. CNC colloidal solution at 2.5 wt % was sonicated for 15 min using the Misonix ultrasonicator. *tert*-Butyl acrylate (*t*BA, 98%) monomer was purchased from Sigma-Aldrich and distilled over calcium hydride. (3-Aminopropyl)triethoxysilane (APTES, ≥98%), trimethylamine (TEA, ≥99%), α-bromoisobutyryl bromide (BIBB, 98%), *N*,*N*,*N*′,*N*″,*N*″-pentamethyldiethylenetriamine (PMDETA, 99%), trifluoroacetic acid (TFA, 99%), ethylenediaminetetraacetic acid (EDTA, ≥99%), and dialysis tubing of the cellulose membrane (with a cutoff molecular weight of 14 kDa) were purchased from Sigma-Aldrich and used as received. Ethanol, dimethylformamide, acetone, and dichloromethane were ACS grade solvents (Pharmco-Aaper) and used without further purification. Hydrochloric acid (ACS reagent grade, 36.5−38%) and sodium hydroxide (97%, Sigma-Aldrich) were used to change the pH of the suspension. Hydrofluoric acid (HF, 99.99%) from Thermo Scientific was used for etching grafted poly(*tert*-butyl acrylate) (P*t*BA) chains from CNC. Calcium chloride from ACE Scientific Inc. was used to eliminate residual HF acid after etching. Deionized (DI) water (18.2 MΩ/cm, Direct-Q Millipore) was used in all of the aqueous solutions. Copper wire (99%) purchased from Amazon was polished with sandpaper and thoroughly cleaned before use. PAA-grafted CNC samples prepared for this study are listed below, and their synthesis is described in the following. Our two samples synthesized for this work are both at the semidilute polymer brush conformation (SDBP) regime.[21] This information will help in understanding the rheological properties of CNC colloids in the following sections.

The APTES-functionalized CNC was prepared following the reported protocol[31] and dispersed in 40 mL DMF. After cooling in an ice-water bath, varying amounts of TEA were added quickly, and BIBB was added dropwise into the flask. The solution was magnetically stirred in an ice bath for 30 min and then at room temperature for 12 h. The nanoparticles (BrCNC−Br) were purified by three centrifugation cycles in DMF and then in acetone. CNC−Br was dispersed in 20 mL of acetone and sonicated until it was well dispersed. CNC−Br in acetone (20 mL) and the *t*BA monomer (20 mL) were mixed in a Schlenk flask. Fifteen cm of copper wire wrapped onto a magnetic stir bar was placed into the flask. Varying amounts of PMDETA were added, and the flask was tightly sealed. The reactant was stirred at 60 °C for varying times, and then the reaction was terminated by cooling it in ice. CNC grafted with P*t*BA (P*t*BA-grafted CNC) was washed and centrifuged in acetone and later in CH_2Cl_2 and finally dispersed in CH_2Cl_2 (40 mL) by sonication.

TFA (3.8 mL) was added into the P*t*BA-grafted CNC in dichloromethane, and the mixture was stirred at room temperature for 24 h. After this hydrolysis step, PAA-grafted CNCs were washed with dichloromethane and DI water several times and collected by centrifugation. The particles were then dialyzed against an aqueous solution of EDTA (1 g/L) in a volume of 1000 mL and then dialyzed in DI water to remove any impurities.

Fourier Transform Infrared (FTIR) Spectroscopy and Thermogravimetric Analysis

The formation of P*t*BA-grafted CNC and the hydrolysis to PAA-grafted CNC were confirmed by using a Bruker Tensor 27 FTIR spectrometer with a resolution of 4 cm^{-1} and 24 scans for each sample. Figure S1 shows the FTIR data of bare CNC, P*t*BA-grafted CNC, and PAA-grafted CNC. Successful hydrolysis of P*t*BA was confirmed with the disappearance of the *tert*-butyl peaks at 1394 and 1369 cm^{-1}. The mass fraction of core CNC and grafted polymer was obtained by a thermogravimetric analyzer (TGA Q50, TA Instruments). Thermogravimetric analysis (TGA) data of bare CNC and its grafted forms are presented in Figure S2.

Measuring Molecular Weights

The molecular weight of P*t*BA was measured by a gel permeation chromatography/light scattering (GPC/LS) system equipped with a Varian PL 5 μm mixed-C gel column, a miniDAWN TREOS light scattering detector, and an Optilab rEX refractometer (Wyatt Technology). Specific refractive index increment (d*n*/d*c*) of the P*t*BA polymer in toluene was found to be −0.036 mL/g. 2 mL of P*t*BA-grafted CNC in toluene suspension with a concentration of 50 mg/mL was placed into a centrifuge tube, and 4 drops of HF were added. The GPC traces of the two batches of P*t*BA for the PAA−CNC samples used in this work are presented in Figure S3. The data were processed using the Wyatt ASTRA software. The supernatant of the centrifuged solution is traditionally analyzed to measure the free-chain molecular weight. In surface-initiated polymerization, some unbound initiator in the solution forms the free chains. We measured the molecular weight of HF-etched samples and compared it to the molecular weights of the free chains collected in the supernatant after centrifugation. If polymerization kinetics of free chains is different than the surface-initiated grafted polymer, then one would notice different molecular weights with bimodal feature. Here, we note that the molecular weights of the free chains were quite similar to those of CNC-grafted chains, and the data is displayed in Table S1.

https://doi.org/10.1021/acsaenm.3c00378
ACS Appl. Eng. Mater. XXXX, XXX, XXX−XXX

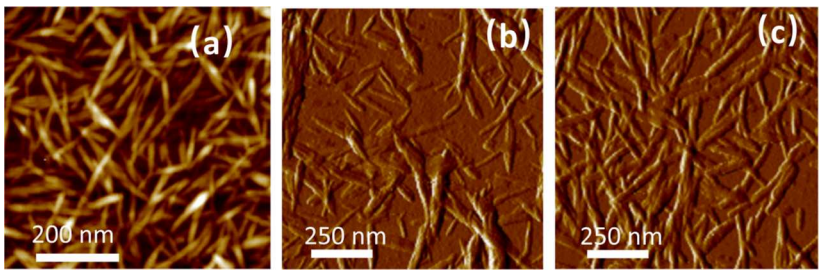

Figure 1. AFM images of (a) bare CNC, (b) 37k PAA−CNC, and (c) 85k PAA−CNC.

Atomic Force Microscopy (AFM)

Bare CNC and PAA-grafted CNC dimensions were investigated by a Bruker BioScope atomic force microscope in non-contact mode.

DLS Measurements

0.03 mg/mL of PAA−CNC solution in DI water was treated with acid and base to adjust their pH measured by an MU 6100 H multimeter (VWR), and diffusivities were measured in a Zetasizer Nano-ZS (Malvern Instruments) at 25 °C. The dichroic film polarizer sheet LPVISE 2 × 2 for 400−700 nm wavelength was purchased from Thorlabs to linearly polarize the low-power laser beam.

Rheological Measurements

6 mg/mL CNC solutions in DI water for rheology measurements were prepared and tested by using an ARES-G2 rheometer (TA Instruments) with a concentric cylinder geometry. Complex viscosity was measured in frequency sweeps with 50% strain for 85k PAA−CNC and with 250% for the 37k PAA−CNC sample. Oscillatory strain sweep measurements were performed at 1 rad/s. Both frequency and strain sweep measurements were conducted at 25 °C.

RESULTS AND DISCUSSION

Critical Concentration of CNC Suspension

CNC rods can freely rotate under shear flow below the critical overlap concentration (C^*). Hydrolyzed CNCs with 145 nm length l_c and 8.5 nm diameter d_c were used in this study. These dimensions provided by the company were also confirmed by AFM. Bare CNC and its PAA-grafted forms were imaged by AFM (Figure 1). C^* was calculated as 5.7 mg/mL using the equation $C^* = \frac{\rho\pi d_c^2}{2.828 l_c^2}$, where ρ = 1.52 g/cm^3 is the density of CNCs. The C^* equation in ref 38 was modified slightly assuming rods occupy spherical spaces that are close-packed.

C^* was determined from the concentration-dependent viscosity measurements on solutions. The phase transition of CNC suspensions as a function of CNC concentration was previously studied in solution rheology.[39] Figure 2 compares the change in the normalized viscosity versus the CNC concentration. The normalized viscosity represents the deviation of viscosity at specified shear rates from that measured at a 200 s^{-1} shear rate. As is seen, the viscosity ratio is 1 for low concentrations, and it increases with decreasing shear rate at high concentrations. The critical concentration where the normalized viscosity deviates from 1 represents the C^*. The measured value of $C^* \sim 6$ mg/mL (0.6 wt %) in Figure 2 matches the calculated C^*, 5.7 mg/mL (0.57 wt %).

Grafted CNC solutions prepared for DLS measurements are very dilute and contained 0.03 mg/mL CNCs. The intensity−intensity autocorrelation function $g_2(t) - 1$ was directly measured by the conventional DLS with one vertical polarizer on an incidence laser beam, known as the vertical−unpolarized

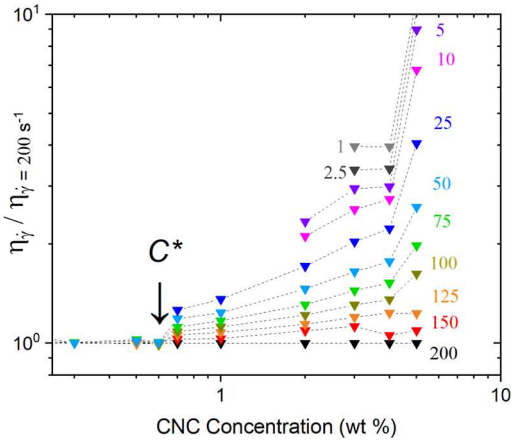

Figure 2. Normalized viscosity ($\eta_{\dot\gamma}/\eta_{200\ s^{-1}}$) of bare CNC solutions as a function of CNC concentration. $\eta_{\dot\gamma}$ represents the viscosity measured under different shear rates, $\dot\gamma$: 1−200 s^{-1}.

(V−U) mode at 25 °C. The translational diffusion coefficient D_t was obtained with this mode.

The pK_a value of sulfate half-ester groups of CNC surface was 2; therefore, the sulfate half-ester groups can be ionized within the wide pH range of 3−11.[40] The repulsive electrostatic force from negatively charged sulfate half-ester groups kept CNCs dispersed, as seen with the overlapped curves for different pH values in bare CNCs (Figure 3a). The pH effect on dispersing CNCs is clearly seen in Figure 3b. CNCs are more aggregated at pH 3, wherein chains are neutral. As chains are stretched between pH 5 and 9 due to ionization, the average size of particles remains quite similar. At pH 11, an excess amount of sodium cations screen the intramolecular repulsive force, and grafted chains collapse on CNC surfaces. The repulsive forces are diminished at pH 11, and the autocorrelation curve becomes like the bare CNC.

Using the equation $g_2(t) = B\{1 + \beta\ [g_1\ (t)]^2\}$, the electric field autocorrelation function (EFACF) $g_1(t)$ is obtained. The equation $g_1\ (t) = \exp(-\Gamma t)$ is used to calculate the decay constant Γ for the ideal monomodal samples. EFACF for polydispersed samples is fitted by the exponential stretching model to calculate the decay constants, Γ_1 and Γ_2, by the following equation[34] $g_1(t) = A_1\ (\exp(-\Gamma_1 t)) + A_2\ \{\exp(-\Gamma_2 t)\}^{\alpha} + B$. A_1, Γ_1, and A_2, Γ_2 are fitting parameters at short times and long times, respectively. Γ_1 is the fast decay rate and A_1 is the fraction of fast events. Γ_2 is the slow decay rate and A_2 represents the fraction of slow events, and α is the stretching exponent. The initial values of all factors are A_1 = 0.99, $A_2 = 1 - A_1$, Γ_1 = 100, Γ_2 = 1, and α = 1. Fitting curves to the raw data of bare CNC and PAA-grafted CNC samples are shown in Figure 4, and the fitting parameters are presented in Table S2. As seen in Table S2, A_1 is found to be much larger than A_2 in

https://doi.org/10.1021/acsaenm.3c00378
ACS Appl. Eng. Mater. XXXX, XXX, XXX−XXX

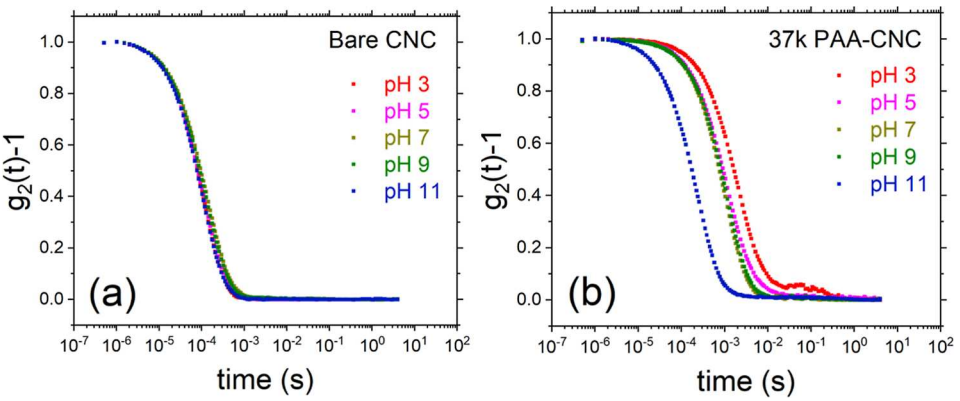

Figure 3. Intensity−intensity autocorrelation function plots presenting the CNC relaxation differences of (a) bare CNC and (b) 37k PAA−CNC at different pH values.

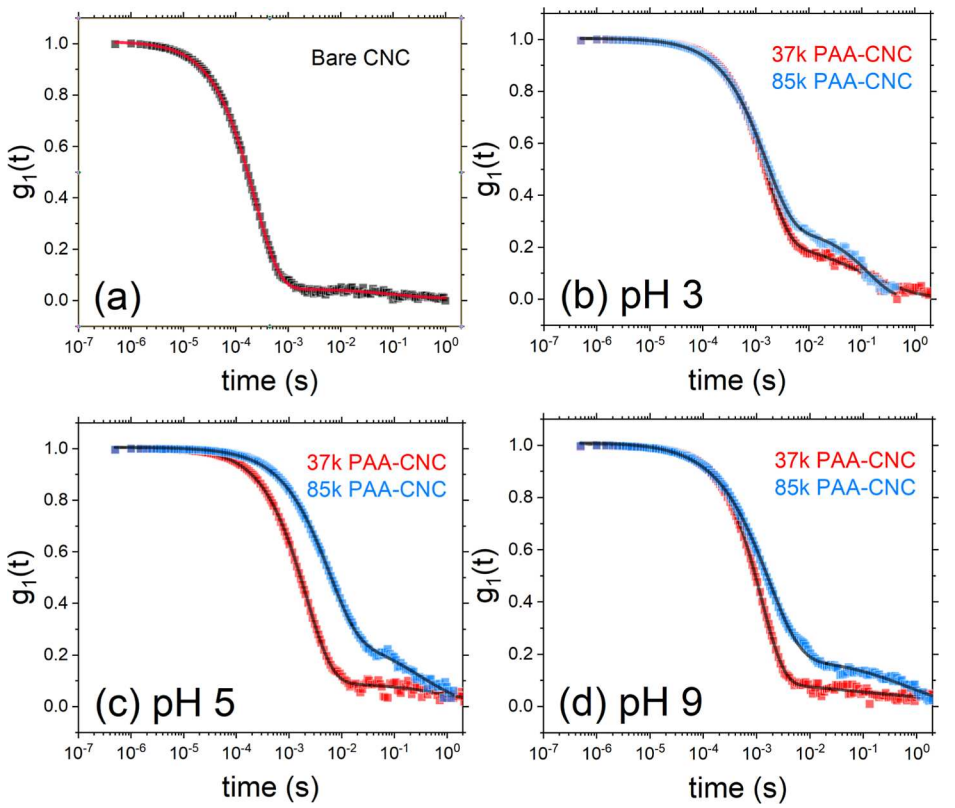

Figure 4. Exponential stretched fit to the intensity−intensity autocorrelation data of (a) bare CNC and (b−d) 37k and 85k PAA−CNC samples at (b) pH 3, (c) pH 5, and (d) pH 9.

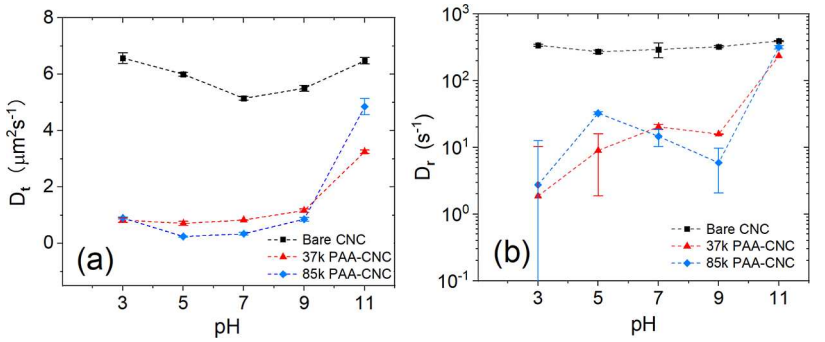

Figure 5. (a) Translational diffusion coefficient D_t and (b) rotational diffusion coefficient D_r of bare CNC and 37k and 85k PAA-grafted CNC samples between pH 3 and 11.

https://doi.org/10.1021/acsaenm.3c00378
ACS Appl. Eng. Mater. XXXX, XXX, XXX−XXX

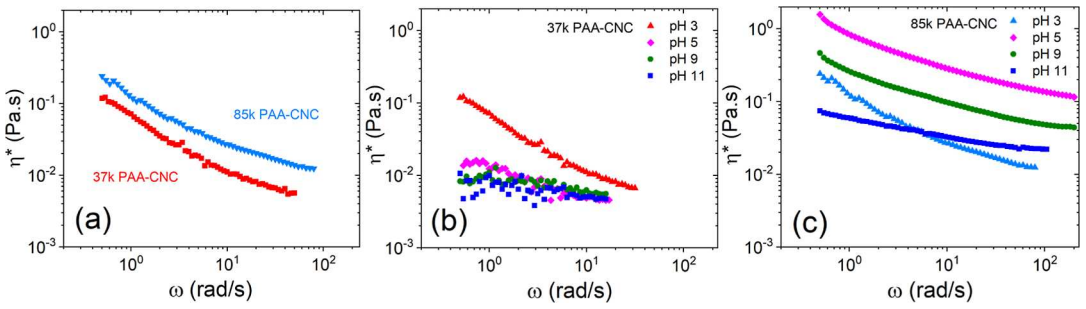

Figure 6. Complex viscosity η^* of (a) 37k PAA−CNC and 85k PAA−CNC solutions at 6 mg/mL concentrations at pH 3 and of (b) 37k PAA−CNC and (c) 85k PAA−CNC solutions with different pH values as a function of frequency.

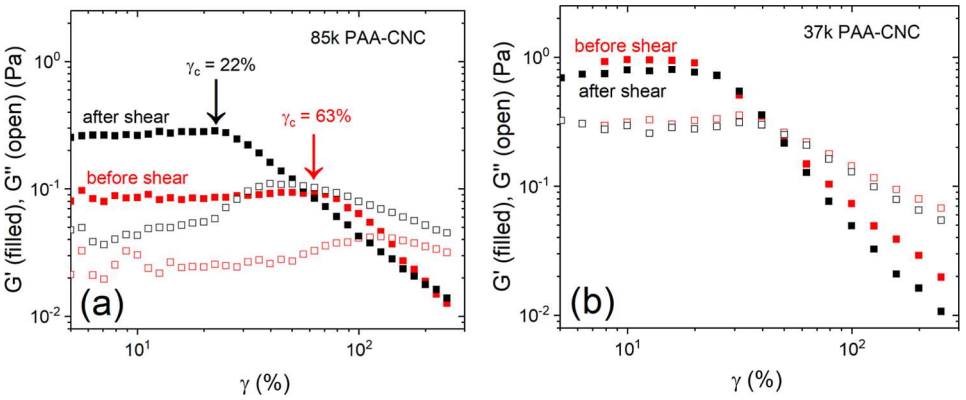

Figure 7. Strain sweep data of (a) 85k and (b) 37k PAA-grafted CNC samples at 6 mg/mL concentration before and after applying 200 s^{-1} shear rate at pH 3. The arrows show the onset of nonlinearity with critical strain values.

all studied samples, suggesting fast diffusion of small particles in solution. Therefore, Γ_1 is used to calculate the translational and rotational diffusivities.

At pH 3, the 37k PAA-grafted CNC sample shows the slowest decay (Figure 4b) because interpenetration of neutral PAA on lower-grafting-density fillers hinders the Brownian motion. At pH 5 (Figure 4c), PAA-grafted CNC formed a larger size of aggregated structure with the long chains (85k) because of the strong hydrogen bonds generated between ionized and un-ionized −COOH groups. At pH 9, the carboxyl group on PAA chains is completely ionized,[27] and the grafted brushes are fully stretched. The interparticle repulsive force prevents the aggregation of CNCs (Figure 4d). Translational diffusion coefficient D_t is calculated using the equation $\Gamma = D_t q^2$. D_t values of all grafted CNC samples are lower than the bare CNC between pH 3 and 5, and their diffusivity reached that of the bare CNC at pH 11 (Figure 5).

The rotational diffusion coefficient D_r was measured in the vertical−horizontal (V−H) mode, where data are collected by adding a horizontal polarizer placed before the detector. The depolarized DLS was calculated by the equation[41] $D_r = (\Gamma_{VH} - \Gamma_{VU})/6$. Γ_{VU} and Γ_{VH} are the decay rates from the V−U mode and the V−H mode, respectively (Figure 5). The measured translational (D_t = 6.5 $\mu m^2/s$) and rotational (D_r = 400 s^{-1}) diffusion coefficients for the bare CNC (l_c: 145 nm in length and d_c: 8.5 nm in width) are lower than the values reported in a published work.[41] This may be due to the variation of dispersion of our bare CNC. Grafted chains hinder both rotational and translational movements, and both diffusivities followed a moderately similar trend such that pH does not affect the translational movements, and chain interactions do not play any role in measured diffusivities. The rotational diffusivities scatter more, yet remain lower than the rotational diffusivity of bare CNC.

6 mg/mL CNC solutions in DI water solutions were tested in frequency sweep runs using an ARES-G2 rheometer. The complex viscosities of all grafted solutions clearly have higher viscosities compared to the bare CNC, and the 85k sample has slightly higher viscosity than the 37k sample (Figure 6a). Hydrogen bonding interactions as described in partially ionized PAA 85k grafts at pH 5 and 9 cause viscosities higher than those at pH 3. At the neutral state, viscosity is lower, as these interactions do not exist at pH 3. The lowest viscosity at pH 11 is attributed to the collapse of PAA chains; hence, the possibility of interparticle interactions through entanglements and hydrogen bonding is diminished.

Strain sweep experiments were carried out on PAA-grafted CNC samples at 25 °C. In the linear region, the gelation response in both grafted systems was observed at pH 3 (Figure 7). The critical strain of the 37k sample was measured to be lower than the 85k sample because chains are less crowded, thus the structural distortion of CNC appears at a low critical strain. The lower modulus of 85k sample may be related to the CNC structures and alignment in this sample. To elucidate the alignment of CNC rods under shear flow, we applied a large shear rate $\dot{\gamma}$ = 200 s^{-1} for 2 min to test if the critical strain changes with structural distortion or the alignment of CNC. It is expected that any decrease in critical strain under shear flow is due to the deformation of grafted chains or breaking of the aligned CNC. We found that entanglements between chains facilitated the network formation, and the long (85k) PAA graft sample became more elastic after applying steady shear (Figure 7a). As the amplitude of strain increased, G' began to decrease and G'' reached a maximum at the higher strain

https://doi.org/10.1021/acsaenm.3c00378
ACS Appl. Eng. Mater. XXXX, XXX, XXX−XXX

amplitude, which is known to be a measure of yield stress.[42,43] The observed crossover of $G'' > G'$ indicates the yielding point of the material. The strain overshoot in the loss modulus (G'') in both before and after shear applied samples indicated that the underlying preformed network formation of the PAA-grafted CNC sample was disrupted by steady shear flow as shown with the lower critical strain value. This preformed network is explained by the formation of weak structures through hydrogen bonding interactions or by entanglements. The weak interactions between PAA chains can be disrupted and rearranged by large deformation, which give rise to strain overshoot in G''. This behavior is similar to what happens in weak gels, as chains temporarily deform and re-entangle. In addition, viscoelastic moduli of the long graft sample enhanced after applying shear and its critical strain decreased (shown by black data points in Figure 7a). These results suggest that CNC rods were disordered (random) before shear and chains entangled effectively as they are at semidilute brush conformation and possibly aligned after steady shear application. The strain overshoot and modulus changes were not observed in short (37k) graft chains (Figure 7b). This reinforcement behavior after shearing was shown on another grafted CNC sample with 127k PAA. The critical strain of 127k PAA sample after shear was also lower than the preshear form (Figure S4). The strong ionization of long (85k) chains at pH 9 lowered the modulus values (Figure S5a), and no significant modulus enhancement was seen after shear; rather, both short- and long-graft samples behaved like a liquid at pH 9 (Figures S5b). The good stability of CNC rods and strong repulsion of ionized chains dominated the chain entanglements and interactions between rods.

CONCLUSIONS

The successful growth of long PAA chains on CNCs provided good stability for CNC rods in water, and this was verified by measuring two modes of diffusion of very dilute PAA-grafted CNC solutions in water. PAA-grafted CNC solutions were characterized for their translational and rotational diffusivities, and the results showed that both diffusivities were slower than the bare CNC. Translational diffusivities of PAA-grafted rods remained constant across a wide pH range of 3−9, showing good stabilization of CNCs with PAA grafting in water. At pH 11, the diffusion reached the diffusivity value of bare CNC in water. Grafted chain length was shown to increase the viscosity of CNC suspensions at the overlap concentration of CNC. The grafted CNCs exhibited an elastic response due to chain entanglements and bridging at the neutral state (pH 3). PAA-grafted CNC showed a more gel-like response when chains were ionized. The chain entanglements and hydrogen bonding interactions created a stronger network of CNC at pH 5−9. The critical strain value for the long-graft chains was measured to be smaller after the steady shear flow. This response is explained by the alignment of CNC under a large shear at pH 3. By comparing long- and short-graft chains with their ionized forms, we conclude that the alignment of CNC helps in the entanglements, creating a stronger network. These findings are critical for establishing processing conditions of polyelectrolyte-grafted CNC colloidal rods in the production of films intended for various applications such as electrochemical sensing, biosensing, and drug delivery.

ASSOCIATED CONTENT

Supporting Information

The Supporting Information is available free of charge at https://pubs.acs.org/doi/10.1021/acsaenm.3c00378.

FTIR spectra of bare CNC, P*t*BA-grafted CNC, and PAA-grafted CNC; TGA data of the synthesized PAA-grafted CNC samples; GPC/LS data of P*t*BA; strain sweep data of 127k PAA−CNC, 85k PAA−CNC, and 37k PAA−CNC samples before and after applying 200 s^{-1} shear rate at pH 3 and pH 9; and stretched exponential fitting parameters to the DLS data (PDF)

AUTHOR INFORMATION

Corresponding Author

Pinar Akcora − *Department of Chemical Engineering and Materials Science, Stevens Institute of Technology, Hoboken, New Jersey 07030, United States;* orcid.org/0000-0001-7853-7201; Email: pakcora@stevens.edu

Author

Yang Ge − *Department of Chemical Engineering and Materials Science, Stevens Institute of Technology, Hoboken, New Jersey 07030, United States*

Complete contact information is available at: https://pubs.acs.org/10.1021/acsaenm.3c00378

Notes

The authors declare no competing financial interest.

ACKNOWLEDGMENTS

We acknowledge the NSF DMR award no. 2104924 for partial financial support.

REFERENCES

(1) Herrera, M. A.; Mathew, A. P.; Oksman, K. Gas permeability and selectivity of cellulose nanocrystals films (layers) deposited by spin coating. *Carbohydr. Polym.* **2014**, *112*, 494−501.

(2) Lee, K. Y.; Aitomäki, Y.; Berglund, L. A.; Oksman, K.; Bismarck, A. On the use of nanocellulose as reinforcement in polymer matrix composites. *Compos. Sci. Technol.* **2014**, *105*, 15−27.

(3) Mariano, M.; El Kissi, N.; Dufresne, A. Cellulose nanocrystals and related nanocomposites: Review of some properties and challenges. *J. Polym. Sci., Part B: Polym. Phys.* **2014**, *52* (12), 791−806.

(4) Oksman, K.; Aitomäki, Y.; Mathew, A. P.; Siqueira, G.; Zhou, Q.; Butylina, S.; Tanpichai, S.; Zhou, X.; Hooshmand, S. Review of the recent developments in cellulose nanocomposite processing. *Composites, Part A* **2016**, *83*, 2−18.

(5) Tan, C.; Peng, J.; Lin, W.; Xing, Y.; Xu, K.; Wu, J.; Chen, M. Role of surface modification and mechanical orientation on property enhancement of cellulose nanocrystals/polymer nanocomposites. *Eur. Polym. J.* **2015**, *62*, 186−197.

(6) Engkagul, V.; Rader, C.; Pon, N.; Rowan, S. J.; Weder, C. Nanocomposites Assembled via Electrostatic Interactions between Cellulose Nanocrystals and a Cationic Polymer. *Biomacromolecules* **2021**, *22* (12), 5087−5096.

(7) Calvino, C.; Macke, N.; Kato, R.; Rowan, S. J. Development, processing and applications of bio-sourced cellulose nanocrystal composites. *Prog. Polym. Sci.* **2020**, *103*, 101221.

(8) Shojaeiarani, J.; Bajwa, D. S.; Chanda, S. Cellulose nanocrystal based composites: A review. *Compos., Part C: Open Access* **2021**, *5*, 100164.

(9) Abbasi Moud, A. Chiral Liquid Crystalline Properties of Cellulose Nanocrystals: Fundamentals and Applications. *ACS Omega* **2022**, *7* (35), 30673−30699.
(10) Qu, D.; Zussman, E. Electro-responsive Liquid Crystalline Nanocelluloses with Reversible Switching. *J. Phys. Chem. Lett.* **2020**, *11* (16), 6697−6703.
(11) Revol, J. F.; Bradford, H.; Giasson, J.; Marchessault, R. H.; Gray, D. G. Helicoidal self-ordering of cellulose microfibrils in aqueous suspension. *Int. J. Biol. Macromol.* **1992**, *14* (3), 170−172.
(12) Revol, J. F.; Godbout, L.; Dong, X. M.; Gray, D. G.; Chanzy, H.; Maret, G. Chiral nematic suspensions of cellulose crystallites; phase separation and magnetic field orientation. *Liq. Cryst.* **1994**, *16* (1), 127−134.
(13) Klockars, K. W.; Tardy, B. L.; Borghei, M.; Tripathi, A.; Greca, L. G.; Rojas, O. J. Effect of Anisotropy of Cellulose Nanocrystal Suspensions on Stratification, Domain Structure Formation, and Structural Colors. *Biomacromolecules* **2018**, *19* (7), 2931−2943.
(14) Lin, M.; Singh Raghuwanshi, V.; Browne, C.; Simon, G. P.; Garnier, G. Modulating the chiral nanoarchitecture of cellulose nanocrystals through interaction with salts and polymer. *J. Colloid Interface Sci.* **2022**, *613*, 207−217.
(15) Cheung, C. C. Y.; Giese, M.; Kelly, J. A.; Hamad, W. Y.; Maclachlan, M. J. Iridescent chiral nematic cellulose nanocrystal/polymer composites assembled in organic solvents. *ACS Macro Lett.* **2013**, *2* (11), 1016−1020.
(16) Chang, H.; Luo, J.; Bakhtiary Davijani, A. A.; Chien, A. T.; Wang, P. H.; Liu, H. C.; Kumar, S. Individually Dispersed Wood-Based Cellulose Nanocrystals. *ACS Appl. Mater. Interfaces* **2016**, *8* (9), 5768−5771.
(17) Hoeng, F.; Denneulin, A.; Neuman, C.; Bras, J. Charge density modification of carboxylated cellulose nanocrystals for stable silver nanoparticles suspension preparation. *J. Nanopart. Res.* **2015**, *17* (6), 244.
(18) Olivier, C.; Moreau, C.; Bertoncini, P.; Bizot, H.; Chauvet, O.; Cathala, B. Cellulose nanocrystal-assisted dispersion of luminescent single-walled carbon nanotubes for layer-by-layer assembled hybrid thin films. *Langmuir* **2012**, *28* (34), 12463−12471.
(19) Rezayat, M.; Blundell, R. K.; Camp, J. E.; Walsh, D. A.; Thielemans, W. Green one-step synthesis of catalytically active palladium nanoparticles supported on cellulose nanocrystals. *ACS Sustainable Chem. Eng.* **2014**, *2* (5), 1241−1250.
(20) Nie, J.; Mou, W.; Ding, J.; Chen, Y. Bio-based epoxidized natural rubber/chitin nanocrystals composites: Self-healing and enhanced mechanical properties. *Composites, Part B* **2019**, *172*, 152−160.
(21) Lettow, J. H.; Yang, H.; Nealey, P. F.; Rowan, S. J. Effect of Graft Molecular Weight and Density on the Mechanical Properties of Polystyrene-Grafted Cellulose Nanocrystal Films. *Macromolecules* **2021**, *54* (22), 10594−10604.
(22) Klein, J. Molecular mechanisms of synovial joint lubrication. *Proc. Inst. Mech. Eng., Part J* **2006**, *220* (8), 691−710.
(23) Cringus-Fundeanu, I.; Luijten, J.; Van Der Mei, H. C.; Busscher, H. J.; Schouten, A. J. Synthesis and characterization of surface-grafted polyacrylamide brushes and their inhibition of microbial adhesion. *Langmuir* **2007**, *23* (9), 5120−5126.
(24) Liu, Y.; Xu, H.; Zhou, L.; Zhang, J. Highly efficient grafting of polyvinyl acetate onto cellulose nanocrystals in the aqueous phase. *Green Chem.* **2023**, *25* (8), 3027−3033.
(25) Ge, Y.; Lin, N.; Du, C.; Amann, T.; Feng, H.; Yuan, C.; Li, K. Improved boundary lubrication of perfluoropolyether using fluoropolymer-grafted cellulose nanocrystal. *Cellulose* **2023**, *30* (6), 3757−3771.
(26) Tang, C.; Spinney, S.; Shi, Z.; Tang, J.; Peng, B.; Luo, J.; Tam, K. C. Amphiphilic Cellulose Nanocrystals for Enhanced Pickering Emulsion Stabilization. *Langmuir* **2018**, *34* (43), 12897−12905.
(27) Choi, J.; Rubner, M. F. Influence of the degree of ionization on weak polyelectrolyte multilayer assembly. *Macromolecules* **2005**, *38* (1), 116−124.
(28) Li, B.; Xu, L.; Wu, Q.; Chen, T.; Sun, P.; Jin, Q.; Ding, D.; Wang, X.; Xue, G.; Shi, A. C. Various types of hydrogen bonds, their temperature dependence and water - Polymer interaction in hydrated poly(acrylic acid) as revealed by1H solid-state NMR spectroscopy. *Macromolecules* **2007**, *40* (16), 5776−5786.
(29) Zhulina, E. B.; Rubinstein, M. Lubrication by polyelectrolyte brushes. *Macromolecules* **2014**, *47* (16), 5825−5838.
(30) Raviv, U.; Giasson, S.; Kampf, N.; Gohy, J. F.; Jérôme, R.; Klein, J. Lubrication by charged polymers. *Nature* **2003**, *425* (6954), 163−165.
(31) Zhang, C.; Yang, S.; Padmanabhan, V.; Akcora, P. Solution Rheology of Poly(acrylic acid)-Grafted Silica Nanoparticles. *Macromolecules* **2019**, *52* (24), 9594−9603.
(32) Calabrese, V.; Varchanis, S.; Haward, S. J.; Shen, A. Q. Alignment of Colloidal Rods in Crowded Environments. *Macromolecules* **2022**, *55* (13), 5610−5620.
(33) Alam, S.; Mukhopadhyay, A. Translational and rotational diffusions of nanorods within semidilute and entangled polymer solutions. *Macromolecules* **2014**, *47* (19), 6919−6924.
(34) Esmaeili, M.; George, K.; Rezvan, G.; Taheri-Qazvini, N.; Zhang, R.; Sadati, M. Capillary Flow Characterizations of Chiral Nematic Cellulose Nanocrystal Suspensions. *Langmuir* **2022**, *38* (7), 2192−2204.
(35) Hausmann, M. K.; Rühs, P. A.; Siqueira, G.; Läuger, J.; Libanori, R.; Zimmermann, T.; Studart, A. R. Dynamics of Cellulose Nanocrystal Alignment during 3D Printing. *ACS Nano* **2018**, *12* (7), 6926−6937.
(36) Hobbie, E. K.; Wang, H.; Kim, H.; Lin-Gibson, S.; Grulke, E. A. Orientation of carbon nanotubes in a sheared polymer melt. *Phys. Fluids* **2003**, *15* (5), 1196−1202.
(37) Gunes, D. Z.; Scirocco, R.; Mewis, J.; Vermant, J. Flow-induced orientation of non-spherical particles: Effect of aspect ratio and medium rheology. *J. Non-Newtonian Fluid Mech.* **2008**, *155* (1−2), 39−50.
(38) Qiao, C.; Chen, G.; Zhang, J.; Yao, J. Structure and rheological properties of cellulose nanocrystals suspension. *Food Hydrocolloids* **2016**, *55*, 19−25.
(39) Ureña-Benavides, E. E.; Ao, G.; Davis, V. A.; Kitchens, C. L. Rheology and phase behavior of lyotropic cellulose nanocrystal suspensions. *Macromolecules* **2011**, *44* (22), 8990−8998.
(40) Beck, S.; Méthot, M.; Bouchard, J. General procedure for determining cellulose nanocrystal sulfate half-ester content by conductometric titration. *Cellulose* **2015**, *22* (1), 101−116.
(41) Arai, K.; Horikawa, Y.; Shikata, T. Transport Properties of Commercial Cellulose Nanocrystals in Aqueous Suspension Prepared from Chemical Pulp via Sulfuric Acid Hydrolysis. *ACS Omega* **2018**, *3* (10), 13944−13951.
(42) Shih, W. Y.; Shih, W. H.; Aksay, I. A. Elastic and yield behavior of strongly flocculated colloids. *J. Am. Ceram. Soc.* **2004**, *82* (3), 616−624.
(43) Donley, G. J.; de Bruyn, J. R.; McKinley, G. H.; Rogers, S. A. Time-resolved dynamics of the yielding transition in soft materials. *J. Non-Newtonian Fluid Mech.* **2019**, *264*, 117−134.

https://doi.org/10.1021/acsaenm.3c00378
ACS Appl. Eng. Mater. XXXX, XXX, XXX−XXX